Influence of skin tone on target size detectability in photoacoustic breast imaging

Rhea D. Rasquinha[a], Mardava R. Gubbi[b], and Muyinatu A. Lediju Bell[b,c,d,e*]

[a]Department of Biomedical Engineering, Brown University, Providence, RI
[b]Department of Electrical and Computer Engineering, Johns Hopkins University, Baltimore, MD
[c]Department of Biomedical Engineering, Johns Hopkins University, Baltimore, MD
[d]Department of Computer Science, Johns Hopkins University, Baltimore, MD
[e]Department of Oncology, Johns Hopkins Medicine, Baltimore, MD

ABSTRACT

Photoacoustic imaging has the potential to improve non-invasive breast cancer diagnosis through the detection of vascular structures. However, illumination through skin introduces a skin tone bias, as greater melanin content increases optical absorption and can create acoustic clutter, reducing the visibility of various target sizes. The impact of skin tone bias as a function of target size was investigated when implementing a fast Fourier transform (FFT)-based reconstruction and short-lag spatial coherence (SLSC) beamforming. These two methods were applied to channel data from multidomain simulations with two optical wavelengths (800 nm and 1064 nm), three tan skin tones with individual typology angles (ITAs) ranging 12° to 26° to assess the impact on 11 spherical targets (with diameters ranging 0.5 mm to 3 mm), as well as one dark skin tone (ITA = -45°) and one very light skin tone (ITA = 60°) to assess outcomes with two vessel structure targets. Each of the investigated targets were embedded in a previously validated realistic 3D breast model. The signal-to-noise ratio (SNR) and generalized contrast-to-noise ratio (gCNR) were measured to quantitatively assess target visibility. With 800 and 1064 nm wavelengths, targets underlying tan skin tones were difficult to visualize with FFT beamforming, with mean SNR and gCNR $\leq$4.51 and $\leq$0.61, respectively. SLSC beamforming enabled visualization of simulated target sizes ranging 1.25-3 mm, with mean SNR $\geq$3.47 and mean gCNR $\geq$0.57. These improvements translated to improved visualization of simulated vessel structures derived from *in vivo* photoacoustic images with SLSC beamforming (relative to the FFT reconstruction method). Results are promising to equitably advance next-generation photoacoustic imaging systems for breast cancer diagnosis, considering multiple skin tones.

Keywords: breast imaging, photoacoustic imaging, acoustic clutter, target visibility, coherence-based beamforming

1. INTRODUCTION

Photoacoustic imaging has the potential to improve non-invasive breast cancer diagnosis through the detection of vascular structures. Photoacoustic imaging is based on the photoacoustic effect, by which optical energy is converted to acoustic energy.[1] Current clinical methods for breast cancer screening include x-ray mammography, magnetic resonance imaging, and ultrasound imaging, but these are limited by decreased sensitivity in patients with greater breast density, high cost, and high false positive rates, respectively.[2–6] Photoacoustic imaging can be used to generate high-resolution images, as the scattering of acoustic waves in tissue is significantly less than that of optical waves.[7] However, illumination through skin introduces a skin tone bias, as greater melanin content increases optical absorption and can create acoustic clutter,[8] reducing the visibility of various target sizes. Fernandes *et al.*[8] confirmed skin as the primary source of acoustic clutter.

Short-lag spatial coherence (SLSC) beamforming[9] is an image reconstruction method previously shown to mitigate a skin tone bias in photoacoustic imaging of the radial artery.[10] The low spatial coherence of clutter

Address all correspondence to:
Muyinatu A. Lediju Bell, mledijubell@jhu.edu

Photons Plus Ultrasound: Imaging and Sensing 2025, edited by Alexander A. Oraevsky, Lihong V. Wang, Proc. of SPIE Vol. 13319, 1331914 · © 2025 SPIE
1605-7422 · doi: 10.1117/12.3045642

sources enables the mitigation of clutter artifacts with SLSC beamforming,[11–13] which improves photoacoustic image quality in noisy environments with low optical fluence.[10,14] Our recent journal paper demonstrates that a 1064 nm transmit wavelength combined with SLSC beamforming enabled visualization of target sizes ranging 0.5-3 mm underlying skin tones ranging from very light to dark.[15]

To highlight this achievement, we focus this conference paper on the clutter reduction achieved with five specific skin tones, representing ITA values of -45°, 12°, 20°, 26°, and 60°. These ITA values correspond to the Very Light (ITA = 60°), Tan (ITA = 12°, 20°, 26°), and Dark (ITA = -45°) skin tone categories.[16–18] Tan was chosen as one example of a skin tone category that produces significant acoustic clutter with amplitude-based methods, which can be mitigated with SLSC beamforming.[10,15] The very light and dark skin tone ITA values represent the maximum and minimum of the range of possible skin tones that were previously investigated.[15] Multidomain simulations were performed with 11 representative target sizes, vessel simulation models designed to mimic previously published features of interest,[19] and two wavelengths that are currently used in clinical systems (i.e., 800 nm[19,20] and 1064 nm[20–22]).

2. METHODS

Eleven simulation volumes were constructed using a realistic 3D breast model[23] immersed in water and one spherical photoacoustic target per volume (diameter range: 0.5 mm to 3 mm, in 0.25 mm increments). In addition, two simulation volumes were generated to incorporate splayed and claw vessel structures, which are features of benign and malignant lesions, respectively.[19] The center of each spherical target was placed 8.6 mm from the skin surface in the axial direction of a simulated linear array transducer, which corresponded to 10 mm from the top of the simulation volume. The positions of the vessel structures within the simulation volumes were based on the reference *in vivo* photoacoustic images.[19] The top of the splayed vessel was placed 5.5 mm from the top of the simulation volume. The lateral center of the claw structure was placed 9.5 mm from the top of the simulation volume.

Optical and acoustic simulations were implemented using MCXLAB[24] and k-Wave,[25] respectively. The simulated light source was a Gaussian beam with a 4-mm waist radius emitting 10^8 photons. Simulations were performed with two optical wavelengths (i.e., 800 nm and 1064 nm) and five skin tones (i.e., ITA = 12°, 20°, and 26° for spherical targets and ITA = -45° and 60° for vessel structures). Three ITA values corresponding to the tan skin tone category were chosen for the spherical target simulations to produce examples for which significant acoustic clutter exists with amplitude-based methods, which can be mitigated with SLSC beamforming.[10,15] The ITA values corresponding to the very light and dark skin tone categories for the vessel structure simulations provide comparative examples from the maximum and minimum of the range of possible skin tones that were previously investigated.[15] The initial pressure for the acoustic simulations was computed as $\Phi(\vec{r}) \cdot \mu_a(\vec{r}) \cdot \Gamma$, where $\Phi(\vec{r})$ is the light fluence map derived from the optical simulation, $\mu_a(\vec{r})$ is the optical absorption coefficient map, and Γ is the Grüneisen parameter, which was set to 1. A linear array ultrasound transducer defined with 128 elements, 0.3 mm pitch, and a 7 MHz center frequency was used to record the acoustic pressure. These parameters were utilized to simulate an Ultrasonix L14-5/38 linear array transducer.[26,27] Additive white Gaussian noise corresponding to a 20 dB channel signal-to-noise ration (SNR) was added to the simulated channel data, as some level of background noise is present in most experimental channel data.

Photoacoustic images were generated using amplitude-based beamforming with the fast Fourier transform (FFT)-based reconstruction technique available in k-Wave[25] and SLSC beamforming, according to the equations:[9,14]

$$\hat{R}(m) = \frac{1}{N-m} \sum_{i=1}^{N-m} \frac{\sum_{n=n_1}^{n_2} s_i(n) s_{i+m}(n)}{\sqrt{\sum_{n=n_1}^{n_2} s_i^2(n) \sum_{n=n_1}^{n_2} s_{i+m}^2(n)}}, \tag{1}$$

$$\mathrm{SLSC}_{\mathrm{pixel}} = \sum_{m=1}^{M} \hat{R}(m), \tag{2}$$

where N is the number of receiving elements in the simulated ultrasound transducer, $s_i(n)$ is the zero-mean time-delayed signal received by the ith transducer element at a depth of n samples, n_1 to n_2 is the size of the correlation kernel, and $\hat{R}(m)$ is the normalized spatial correlation between $s_i(n)$ and $s_{i+m}(n)$ for a given spatial lag (defined in terms of element separation) m. To calculate the displayed and analyzed SLSC images, tunable parameters were fixed (e.g., $M = 10$, axial correlation kernel length equal to one acoustic wavelength), and each photoacoustic image was normalized to its brightest pixel. SNR and generalized contrast-to-noise ratio (gCNR)[28–30] were measured to quantitatively assess target visibility.

3. RESULTS AND DISCUSSION

Figure 1 shows representative examples of simulated photoacoustic images generated using 800 nm wavelength and FFT and SLSC beamforming, underlying a tan skin tone (ITA = 20°). The ground truth images of the simulation volumes are shown above the images for comparison. With FFT beamforming, target sizes ranging 0.5 mm to 3 mm are difficult to visualize due to the presence of acoustic clutter. The simulated targets are better visualized with SLSC beamforming.

Figure 2 shows the mean ± one standard deviation of SNR and gCNR values as functions of target size per wavelength, per beamforming method. SLSC beamforming generally provided mean SNR ≤8.28 and mean gCNR ≤0.99 with the 800 nm wavelength, with mean SNR ≤8.53 and mean gCNR ≤1 with the 1064 nm wavelength. These values are improved over the mean SNR and gCNR achieved with FFT reconstruction (i.e., mean SNR ≤4.51 and mean gCNR ≤0.47, respectively, with the 800 nm wavelength and mean SNR ≤3.61 and mean gCNR ≤0.61, respectively, with the 1064 nm wavelength). In addition, the greatest improvements in SNR and gCNR values with SLSC beamforming generally occurred with the 1.25-3 mm targets, with corresponding mean SNR ≥3.47 and mean gCNR ≥0.57.

Figure 3 shows FFT and SLSC photoacoustic images of the simulated splayed vessel and claw structures imaged through very light and dark skin tones with 800 nm and 1064 nm wavelengths. With FFT reconstruction,

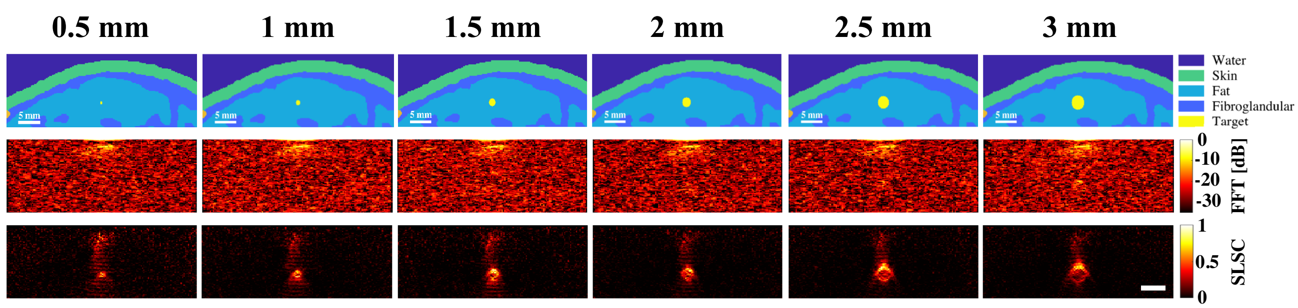

Figure 1. Ground truth images of the simulation volumes, along with photoacoustic images created with 800 nm wavelength, a tan skin tone (ITA = 20°), and FFT and SLSC beamforming.

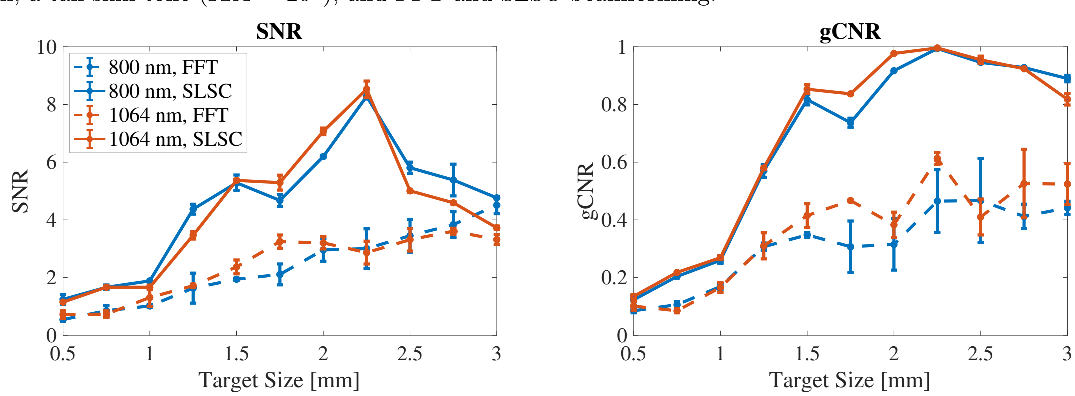

Figure 2. Mean ± one standard deviation of the SNR and gCNR of photoacoustic images created with 800 nm and 1064 nm wavelengths and FFT and SLSC beamforming underlying tan skin tones, displayed as functions of target size.

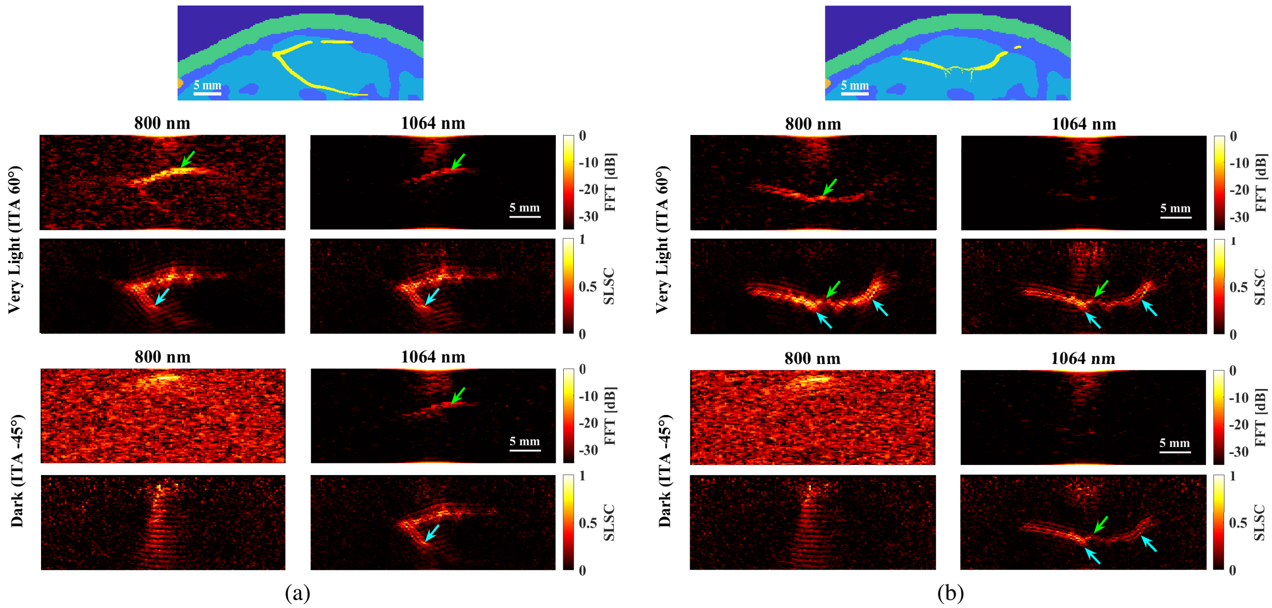

Figure 3. FFT and SLSC photoacoustic images of a (a) splayed vessel and (b) claw structure for very light (ITA=60°) and dark (ITA=-45°) skin tones, visualized with 800 nm and 1064 nm wavelengths. The green arrows indicate vessel components with diameters ≤0.5 mm. The blue arrows indicate vessel components that cannot be visualized in the corresponding FFT images.

the distal vessel of the splayed vessel (0.5-0.75 mm diameter) and the branching vessels in the claw (diameter ≤0.4 mm) are difficult to visualize. However, the blue arrows highlight better visualization of the 0.75 mm-diameter segment of the distal vessel and partial visualization of the branching vessels with SLSC beamforming. For the dark skin tone, the vessel structures can only be visualized with 1064 nm wavelength and SLSC beamforming, for which visualization is comparable to the very light skin tone.

Overall, the SLSC beamformer offers improved target visualization of 0.5-3 mm targets and vessel structures, relative to amplitude-based FFT beamforming results obtained with an 800 nm wavelength. In particular, the clutter present in the FFT images created with tan skin tones is both quantitatively and qualitatively reduced with SLSC beamforming (see Figs. 1 and 2, respectively). It is similarly promising that SLSC beamforming reduced acoustic clutter and increased the visibility of structures underlying very light and dark skin tones with both the 800 nm and 1064 nm wavelengths (Fig. 3). Based on our recent journal paper,[15] similar results are expected for a wider range of skin tones.

4. CONCLUSION

This paper provides direct qualitative and quantitative comparisons of the influence of skin tone on target visibility and detectability, with a focus on very light, tan, and dark skin tones. The SLSC beamformer reduced clutter and improved SNR and gCNR values over FFT beamforming with 800 nm wavelength and tan skin tones. SLSC images of two vessel structures underlying dark skin tones imaged with 1064 nm wavelength were comparable to those of the lightest skin tones imaged with 800 nm and 1064 nm wavelengths. Therefore, SLSC beamforming is a promising approach to address challenges with photoacoustic target visibility when developing technology for patient populations consisting of a range of different skin tones.

ACKNOWLEDGMENTS

This work is supported by grant number 2022-309513 from the Chan Zuckerberg Initiative DAF (an advised fund of Silicon Valley Community Foundation), NIH R01 EB032960, and the NSF Alan T. Waterman Award Number IIS-2431810. This work was also completed in partnership with the NSF Computational Sensing and Medical Robotics Research Experience for Undergraduates program (NSF Grant No. EEC-1852155).

REFERENCES

[1] Xia, J., Yao, J., and Wang, L. V., "Photoacoustic tomography: principles and advances," *Electromagn. Waves (Camb.)* **147**, 1–22 (2014). [doi:10.2528/pier14032303].

[2] Pinsky, R. W. and Helvie, M. A., "Mammographic breast density: effect on imaging and breast cancer risk," *J. Natl. Compr. Canc. Netw.* **8**(10), 1157–1164 (2010). [doi:10.6004/jnccn.2010.0085].

[3] Freer, P. E., "Mammographic breast density: impact on breast cancer risk and implications for screening," *Radiographics* **35**(2), 302–315 (2015). [doi:10.1148/rg.352140106].

[4] Nyayapathi, N. and Xia, J., "Photoacoustic imaging of breast cancer: a mini review of system design and image features," *J. Biomed. Opt.* **24**(12), 1–13 (2019). [doi:10.1117/1.JBO.24.12.121911].

[5] Wiacek, A., Oluyemi, E., Myers, K., Mullen, L., and Bell, M. A. L., "Coherence-based beamforming increases the diagnostic certainty of distinguishing fluid from solid masses in breast ultrasound exams," *Ultrasound Med. Biol.* **46**(6), 1380–1394 (2020). [doi:10.1016/j.ultrasmedbio.2020.01.016].

[6] Pan, I. W., Oeffinger, K. C., and Shih, Y. T., "Cost-sharing and out-of-pocket cost for women who received mri for breast cancer screening," *J. Natl. Cancer Inst.* **114**(2), 254–262 (2022). [doi:10.1093/jnci/djab150].

[7] Wang, L. V. and Wu, H.-i., [*Biomedical optics: principles and imaging*], John Wiley & Sons (2007).

[8] Fernandes, G. S. P., Pavan, T. Z., and Bell, M. A. L., "In silico demonstrations of the impact of wavelength and skin tone on photoacoustic breast imaging," in [*2023 IEEE International Ultrasonics Symposium (IUS)*], 1–4 (2023).

[9] Lediju, M. A., Trahey, G. E., Byram, B. C., and Dahl, J. J., "Short-lag spatial coherence of backscattered echoes: imaging characteristics," *IEEE Trans. Ultrason. Ferroelectr. Freq. Control.* **58**, 1377–1388 (2011). [doi:10.1109/TUFFC.2011.1957].

[10] Fernandes, G. S. P., Uliana, J. H., Bachmann, L., Carneiro, A. A. O., Lediju Bell, M. A., and Pavan, T. Z., "Mitigating skin tone bias in linear array *in vivo* photoacoustic imaging with short-lag spatial coherence beamforming," *Photoacoustics* **33**, 100555 (2023). [doi:10.1016/j.pacs.2023.100555].

[11] Lediju Bell, M. A., Kuo, N., Song, D. Y., and Boctor, E. M., "Short-lag spatial coherence beamforming of photoacoustic images for enhanced visualization of prostate brachytherapy seeds," *Biomed. Opt. Express* **4**(10), 1964–1977 (2013). [doi:10.1364/BOE.4.001964].

[12] Lediju Bell, M. A., Kuo, N. P., Song, D. Y., Kang, J. U., and Boctor, E. M., "*In vivo* visualization of prostate brachytherapy seeds with photoacoustic imaging," *J. Biomed. Opt.* **19**(12), 126011 (2014). [doi:10.1117/1.JBO.19.12.126011].

[13] Lediju Bell, M. A., Guo, X., Kang, H. J., and Boctor, E., "Improved contrast in laser-diode-based photoacoustic images with short-lag spatial coherence beamforming," in [*2014 IEEE International Ultrasonics Symposium*], 37–40 (2014). [doi:10.1109/ULTSYM.2014.0010].

[14] Graham, M. T. and Bell, M. A. L., "Photoacoustic spatial coherence theory and applications to coherence-based image contrast and resolution," *IEEE Trans. Ultrason. Ferroelectr. Freq. Control.* **67**(10), 2069–2084 (2020). [doi:10.1109/TUFFC.2020.2999343.

[15] Rasquinha, R. D., Gubbi, M. R., and Bell, M. A. L., "Impact of skin tone on target size detectability in photoacoustic breast imaging," *Biophotonics Discovery* **2**(1), 012502 (2024). [doi:10.1117/1.BIOS.2.1.012502].

[16] Ly, B. C. K., Dyer, E. B., Feig, J. L., Chien, A. L., and Del Bino, S., "Research techniques made simple: Cutaneous colorimetry: A reliable technique for objective skin color measurement," *J. Inves. Derm.* **140**(1), 3–12.e1 (2020). [doi:10.1016/j.jid.2019.11.003].

[17] Chardon, A., Cretois, I., and Hourseau, C., "Skin colour typology and suntanning pathways," *Int. J. Cosmet. Sci.* **13**(4), 191–208 (1991). [doi:10.1111/j.1467-2494.1991.tb00561.x].

[18] Del Bino, S., Ito, S., Sok, J., Nakanishi, Y., Bastien, P., Wakamatsu, K., and Bernerd, F., "hemical analysis of constitutive pigmentation of human epidermis reveals constant eumelanin to pheomelanin ratio," *Pigment Cell Melanoma Res.* **28**(6), 707–717 (2015). [doi:10.1111/pcmr.12410].

[19] Abeyakoon, O., Woitek, R., Wallis, M. G., Moyle, P. L., Morscher, S., Dahlhaus, N., Ford, S. J., Burton, N. C., Manavaki, R., Mendichovszky, I. A., Joseph, J., Quiros-Gonzalez, I., Bohndiek, S. E., and Gilbert, F. J., "An optoacoustic imaging feature set to characterise blood vessels surrounding benign and malignant breast lesions," *Photoacoustics* **27**, 100383 (2022). [doi:10.1016/j.pacs.2022.100383].

[20] Steinberg, I., Huland, D. M., V., O., Frostig, H. E., Tummers, W. S., and Gambhir, S. S., "Photoacoustic clinical imaging," *Photoacoustics* **14**, 77–98 (2019). [doi:10.1016/j.pacs.2019.05.001].

[21] Manohar, S. and Dantuma, M., "Current and future trends in photoacoustic breast imaging," *Photoacoustics* **16**, 100134 (2019). [doi:10.1016/j.pacs.2019.04.004].

[22] Oraevsky, A. A., Clingman, B., Zalev, J., Stavros, A. T., Yang, W. T., and Parikh, J. R., "Clinical optoacoustic imaging combined with ultrasound for coregistered functional and anatomical mapping of breast tumors," *Photoacoustics* **12**, 30–45 (2018). [doi:10.1016/j.pacs.2018.08.003].

[23] Lou, Y., Zhou, W., Matthews, T. P., Appleton, C. M., and Anastasio, M. A., "Generation of anatomically realistic numerical phantoms for photoacoustic and ultrasonic breast imaging," *J. Biomed Opt.* **22**(4), 41015 (2017). [doi:10.1117/1.JBO.22.4.041015].

[24] Fang, Q. and Boas, D. A., "Monte carlo simulation of photon migration in 3d turbid media accelerated by graphics processing units," *Opt. Express* **17**(22), 20178–20190 (2009). [doi:10.1364/OE.17.020178].

[25] Treeby, B. E. and Cox, B. T., "k-wave: Matlab toolbox for the simulation and reconstruction of photoacoustic wave fields," *J. Biomed. Opt.* **15**(2), 021314 (2010). [doi:10.1117/1.3360308].

[26] Shu, W., Ai, M., Salcudean, T., Rohling, R., Abolmaesumi, P., and Tang, S., "Broadening the detection view of 2d photoacoustic tomography using two linear array transducers," *Opt. Express* **24**(12), 12755–12768 (2016). [doi:https://doi.org/10.1364/OE.24.012755].

[27] Kim, G. R., Kang, J., Kwak, J. Y., Chang, J. H., Kim, S. I., Youk, J. H., Moon, H. J., Kim, M. J., and Kim, E. K., "Photoacoustic imaging of breast microcalcifications: a preliminary study with 8-gauge core-biopsied breast specimens," *PloS One* **9**(8), e105878 (2014). [doi:10.1371/journal.pone.0105878].

[28] Rodriguez-Molares, A., Rindal, O. M. H., D'hooge, J., Masoy, S. E., Austeng, A., Lediju Bell, M. A., and Torp, H., "The generalized contrast-to-noise ratio: A formal definition for lesion detectability," *IEEE Trans. Ultrason. Ferroelectr. Freq. Control* **67**(4), 745–759 (2020). [doi:10.1109/TUFFC.2019.2956855].

[29] Kempski, K. M., Graham, M. T., Gubbi, M. R., Palmer, T., and Lediju Bell, M. A., "Application of the generalized contrast-to-noise ratio to assess photoacoustic image quality," *Biomed. Opt. Express* **11**(7), 3684–3698 (2020). [doi:10.1364/BOE.391026].

[30] Gubbi, M. R., Gonzalez, E. A., and Bell, M. A. L., "Theoretical framework to predict generalized contrast-to-noise ratios of photoacoustic images with applications to computer vision," *IEEE Trans. Ultrason. Ferroelectr. Freq. Control* **69**(6), 2098–2114 (2022). [doi:10.1109/TUFFC.2022.3169082].